

Worked in different universities/institutions in various capacities as follows:

From the Selected Works of Dr. Mohammad Mansoob Khan

April 17, 2014

Biogenic fabrication of Au@CeO₂ nanocomposite with enhanced visible light activity

Mohammad Mansoob Khan, Dr
S. A. Ansari
M. O. Ansari
B. K. Min
J Lee, et al.



SELECTEDWORKS™

Available at: http://works.bepress.com/mmansoob_khan/42/

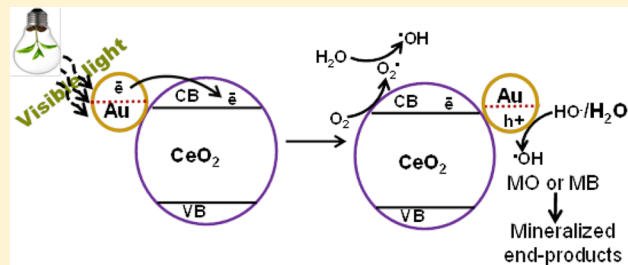
Biogenic Fabrication of Au@CeO₂ Nanocomposite with Enhanced Visible Light Activity

Mohammad Mansoob Khan,[†] Sajid Ali Ansari,[†] Mohd Omaish Ansari,[†] B. K. Min,[‡] Jintae Lee,[†] and Moo Hwan Cho*,[†]

[†]School of Chemical Engineering and [‡]Center for Research Facilities, Yeungnam University, Gyeongsan-si, Gyeongbuk 712-749, South Korea

Supporting Information

ABSTRACT: This study reports a biogenic approach to the synthesis of Au@CeO₂ nanocomposite using electrochemically active biofilms (EABs) in water under normal pressure and 30 °C. This work presents the results of extensive morphological, structural, optical, visible light photoelectrochemical and photocatalytic studies of Au@CeO₂ nanocomposite. The presence of a large number of interfaces between Au nanoparticles and CeO₂ for charge transfer is believed to play a key role in enhancing the optical and visible light photoelectrochemical and photocatalytic performance of Au@CeO₂ nanocomposite. The enhanced visible light degradation of methyl orange and methylene blue by Au@CeO₂ nanocomposite was much higher than that by pure CeO₂. The reusability, stability, and other results suggests that the Au@CeO₂ nanocomposite could be exploited as potential candidates for visible light photocatalysis, photovoltaic, and photoelectrochemical devices.



INTRODUCTION

The development of visible light photoactive materials as an energy carrier that does not use fossil fuels is a great challenge. One of the most attractive options is the use of these materials to harvest solar light on a large scale for a range of technological purposes.¹ A great deal of attention has been devoted to photocatalytic processes because of their applications in many fields, such as environmental remediation, solar energy conversion, and photoelectrochemical processes.² Nanocomposite materials of metal nanoparticles and inorganic semiconductor (metal oxides, such as TiO₂, ZnO, and CeO₂) nanocrystals have attracted considerable attention in the field of materials for solar energy conversion and photoelectrochemical processes because of the possibility of combining the optoelectronic properties of inorganic metal oxides (CeO₂) with the superior conductivity of metal nanoparticles.^{2–4} This is because the power conversion efficiency achievable in single-component solar cells is generally poor. For example, photovoltaic and photoelectrochemical devices based on a semiconductor as the only active material are limited by the extremely low electron mobility.^{2–7} On the other hand, when metal nanoparticles are anchored at an inorganic semiconductor, the performance can undergo from the restricted light fraction and the nanocomposite materials can absorb visible light.^{2–9}

The nature of charge or energy transfer processes between metal nanoparticles and semiconductor nanocrystals depends on the electrical and optical properties of the two materials, surface properties of the nanocrystals, and irradiation wavelength.^{10–12} The efficiency of these nanocomposites is normally

enhanced by decreasing the charge recombination phenomena and band gap narrowing.^{11,12} Metal nanoparticles anchored at the semiconductor surface retard the recombination of photogenerated electron hole pairs, which might be due not only to the attraction of excited electrons to metal nanoparticles, but also to the presence of extra hydroxyl species to delay recombination through hole trapping.^{7–12}

This study reports the biogenic fabrication of Au@CeO₂ nanocomposite, their characterization, visible light photocatalysis, and photoelectrochemical studies, such as electrochemical impedance spectroscopy (EIS) and linear scan voltammetry (LSV) in dark and under visible light irradiation. To the best of the authors' knowledge, this is the first biogenic report for the synthesis and different applications of the Au@CeO₂ nanocomposite. The significance of these finding is 2-fold. This report shows that by using particle sizes down to the nanometer scale, a conventional metal oxide insulator is converted to a semiconductor whose photocatalytic activity strongly dependent on the particle size on the nanometer scale and the quantum confinement effect. Conventional CeO₂ with a large particle size behaves as insulator and lacks any visible light photocatalytic activity.^{3,7} On the other hand, when AuNPs are anchored at CeO₂, it is possible to introduce a visible-light response to the nanocomposite that would otherwise be inactive under visible-light irradiation.

Received: January 27, 2014

Revised: April 16, 2014

Published: April 16, 2014

■ EXPERIMENTAL SECTION

Materials. Chloroauric acid ($\text{HAuCl}_4 \cdot 3.6\text{H}_2\text{O}$) was obtained from Kojima Chemicals, Japan. Cerium oxide (nano CeO_2), methyl orange (MO), and methylene blue (MB) were purchased from Sigma-Aldrich. Sodium acetate, and sodium phosphate were acquired from Duksan Pure Chemicals Co. Ltd., South Korea. Ethyl cellulose and α -terpineol were supplied by KANTO Chemical Co., Japan, and fluorine-doped transparent conducting oxide glass (FTO; F-doped SnO_2 glass; $7\ \Omega/\text{sq}$) was purchased from Pilkington, U.S.A. All other chemicals were of analytical grade and used as received. All solutions were prepared with deionized (DI) water obtained using a PURE ROUP 30 water purification system.

Methods. The UV-vis diffuse absorbance/reflectance spectra (DRS) of the powder $\text{Au}@\text{CeO}_2$ nanocomposite and $\text{P}-\text{CeO}_2$ samples were obtained using a UV-vis-NIR double beam spectrophotometer (VARIAN, Cary 5000, U.S.A.) equipped with a diffuse reflectance accessory. A set amount of the $\text{Au}@\text{CeO}_2$ nanocomposite and $\text{P}-\text{CeO}_2$ powder was pressed uniformly in the sample holder that was placed at the integrating sphere for the reflectance measurements. X-ray diffraction (XRD, PANalytical, X'Pert-PRO MPD) was performed using $\text{Cu K}\alpha$ radiation ($\lambda = 0.15405\ \text{nm}$). The microstructure was examined by field emission transmission electron microscopy (FE-TEM), high resolution TEM (HRTEM), and high angle annular dark field STEM (HAADF-STEM) using Tecnai G2 F20, FEI, U.S.A. The TEM instrument (coefficient of spherical aberration, $\text{Cs} = 1.2\ \text{mm}$) was equipped with a digitally processed STEM image system operating at an accelerating voltage of 200 kV. The TEM was equipped with an EDAX GENESIS energy dispersive system (EDX). The electron diffraction patterns were interpreted using the software Digital Micrograph (Gatan), and crystal structure databases: ICDD PDF 4⁺, Pearson's Crystal Data. X-ray photoelectron spectroscopy (XPS, ESCALAB 250 XPS System, Thermo Fisher Scientific U.K.) was conducted with the following X-ray source: monochromated $\text{Al K}\alpha$; $h\nu = 1486.6\ \text{eV}$; X-ray energy, 15 kV; 150 W; and spot size, $500\ \mu\text{m}$.

The visible light photocatalytic degradation and photoelectrochemical experiments (EIS and LSV) were carried out using a 400 W lamp with an intensity of $31.0\ \text{mW cm}^{-2}$ and $\lambda > 400\ \text{nm}$ (3 M, U.S.A.). The EIS measurements were carried out using a potentiostat (Versa STAT 3, Princeton Research, U.S.A.) with a standard three-electrode system, in which Ag/AgCl (saturated with KCl), a Pt gauge, and FTO glass coated with the as-synthesized $\text{Au}@\text{CeO}_2$ nanocomposite or $\text{P}-\text{CeO}_2$ samples were used as the reference, counter and working photoelectrodes, respectively, in a 0.2 M Na_2SO_4 solution as the electrolyte at room temperature. The projection area of each photoelectrode was $1\ \text{cm}^2$. The experimental conditions for EIS were 0.0 V and a frequency ranging from 1 to $10^4\ \text{Hz}$. The working electrodes for the photoelectrochemical impedance measurements were prepared as follows: 100 mg of each sample was suspended thoroughly by adding ethyl cellulose as the binder and α -terpineol as the solvent for the paste, sonicated for 5 min, and heated with constant stirring to obtain a paste. The resulting paste was coated on a fluorine-doped tin oxide glass (FTO) electrode using a doctor-blade and later dried in an ambient atmosphere.

Development of Electrochemically Active Biofilms. Electrochemically active biofilms (EABs) on carbon paper were

prepared using the procedure reported elsewhere.^{11–17} In short, 0.2 g sodium acetate was added as a substrate to 200 mL of mineral salt medium.^{16,17} This was followed by the addition of 10 mL of anaerobic sludge (Biogas plant in Paju, Republic of South Korea) and sparging with N_2 gas for 5 min to create an anaerobic environment. Finally, carbon paper ($2.5 \times 4.5\ \text{cm}^2$) was dipped into the mixture and the bottle was sealed. All media, including the bacterial inoculum, were changed every 2 days under strict anaerobic conditions. The process was repeated for 2 weeks. The EABs formed on the carbon paper were confirmed using a microbial fuel cell by obtaining the appropriate voltage.¹⁷ The living EABs formed on carbon paper were used to synthesize the $\text{Au}@\text{CeO}_2$ nanocomposite.

EABs Mediated Synthesis of $\text{Au}@\text{CeO}_2$ Nanocomposite. A 5 mM CeO_2 aqueous suspension was prepared. Subsequently, a 1.5 mM HAuCl_4 aqueous solution was added to the reaction mixture with constant stirring. A total of 0.2 g sodium acetate was then added to this suspension as an electron donor. The reaction mixture was sparged with N_2 gas for 5 min to maintain an anaerobic environment. The EAB was hung in the reaction bottle and the system was sealed and left under magnetic stirring at $30\ ^\circ\text{C}$. Within 8 h, the initial white color began to change to a purple-brown color. It is shown in Supporting Information by Figure S1. Finally, a purple-brown precipitate was obtained. The reaction mixture was centrifuged and a powdered $\text{Au}@\text{CeO}_2$ nanocomposite was isolated for further characterization and applications.

Two controlled syntheses were performed to confirm the role of the EAB and sodium acetate. Two 5 mM CeO_2 aqueous suspensions (200 mL) were prepared. In controlled synthesis, a 1.5 mM HAuCl_4 aqueous solution and 0.2 g sodium acetate was added. The reaction mixtures were sparged with N_2 gas for 5 min to maintain the anaerobic conditions. The EAB was hung in the second controlled synthesis only. Both systems were sealed and stirred with a magnetic stirrer at $30\ ^\circ\text{C}$. In both cases, no changes were observed, even after 48 h. This shows that both EAB and sodium acetate are necessary to complete the biogenic reduction reaction.

Visible Light-Mediated Photocatalytic Degradation of MO and MB in the Presence of $\text{Au}@\text{CeO}_2$ Nanocomposite as Photocatalyst. The photocatalytic activities of the as-synthesized $\text{Au}@\text{CeO}_2$ nanocomposite and $\text{P}-\text{CeO}_2$ samples were tested for the degradation of MO and MB under visible light irradiation. The photocatalytic activities of the $\text{Au}@\text{CeO}_2$ nanocomposite and $\text{P}-\text{CeO}_2$ were measured by observing the photodecomposition of MO and MB with a concentration of 10 mg/L. For photodecomposition, 2 mg of each photocatalyst was suspended in 20 mL of a MO and MB aqueous solution. Each solution was sonicated for 5 min in the dark. The solutions were later stirred in the dark for 30 min to reach the adsorption and desorption equilibrium of the specific substrate on the $\text{Au}@\text{CeO}_2$ nanocomposite and $\text{P}-\text{CeO}_2$. Visible light irradiation of the solutions was performed using a 400 W lamp ($\lambda > 400\ \text{nm}$). The two sets of experiments were observed for 6 and 5 h in the case of the MO and MB degradation experiment, respectively. The rate of dye degradation was monitored by taking 1.7 mL of the samples from each set every 1 h, centrifuging them to remove the catalyst and recording the UV-vis spectrum in each case. The MO and MB degradation was calculated using the decrease in the absorbance of the respective degraded solutions.^{11,12}

Two control experiments were performed. In the first controlled experiment, $\text{P}-\text{CeO}_2$ was taken as a reference

photocatalyst to compare the enhanced photocatalytic ability of the Au@CeO₂ nanocomposite. In the second controlled experiment, the photodecomposition of MO and MB was checked without a catalyst only under visible light irradiation. Each experiment was performed in triplicate to ensure the photocatalytic activities of the Au@CeO₂ nanocomposite and P-CeO₂.

Photoelectrochemical Studies of the Au@CeO₂ Nanocomposite. To examine the visible light response of the as-synthesized Au@CeO₂ nanocomposite, photoelectrochemical experiments, such as EIS and LSV, were carried out under ambient conditions in the dark and under visible light irradiation in a 50 mL, 0.2 M Na₂SO₄ aqueous solution at room temperature. For each electrode, first EIS was performed in the dark condition and later under visible light irradiation ($\lambda > 400$ nm) at 0.0 V and with a frequency ranging from 1–10⁴ Hz. Later, the photocurrent response was obtained using LSV in dark and under visible light irradiation at a scan rate of 50 mV/s over the potential range, −1.0 to 1.0 V.

Stability and Reusability of the Au@CeO₂ Nanocomposite. A preliminary test for stability was performed by suspending the Au@CeO₂ nanocomposite in water and sonicating the mixture for 1 h. An analysis of the AuNPs leached in the solution was observed by UV-vis spectrophotometry, which confirmed the stability of the Au@CeO₂ nanocomposite and the possibility of its use as a catalyst. The reusability of the Au@CeO₂ nanocomposite was tested after centrifuging the catalyst from MO and MB degraded solutions. The isolated catalyst from first and second run were washed with DI water, dried in an oven at 100 °C and successively reused for second and third run to check their catalytic activity with a fresh MO and MB solution under the same conditions.

RESULTS AND DISCUSSION

Biogenic Synthesis of Au@CeO₂ Nanocomposite and Characterization. The EABs are well-known in microbial fuel cells and bioinspired nanomaterials synthesis.^{11–18} In this study, this biogenic and green approach was expanded to synthesize the Au@CeO₂ nanocomposite for visible light photocatalysis and photoelectrochemical studies. Figure 1

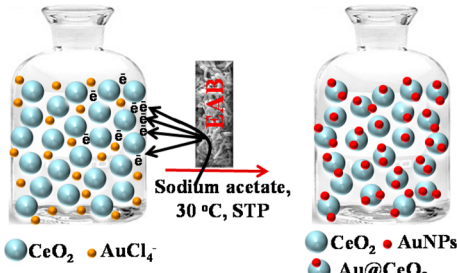


Figure 1. Proposed mechanism for the synthesis of the Au@CeO₂ nanocomposite in the presence of EAB and sodium acetate as an electron donor.

shows the proposed synthesis of the Au@CeO₂ nanocomposite in the presence of EAB and sodium acetate in water at 30 °C. The electrons produced by EAB, after biologically decomposing the acetate, were used in the reduction of Au³⁺ to Au⁰ at the surface of CeO₂, which results in the formation of the Au@CeO₂ nanocomposite. Schematic mechanistic diagram for the synthesis of Au@CeO₂ nanocomposite is shown in Supporting

Information by Figure S1. The product obtained in this synthesis was highly pure as the biofilm was supported on carbon paper. It is well-known that many methods uses hazardous chemical for the synthesis of metal–metal oxide nanocomposites.^{8–10} However, the advantage of this protocol is that it does not involve any external energy input, which makes this synthesis highly useful and efficient in the field of nanocomposite syntheses. Other exciting features of this synthesis is that it takes place in water at room temperature and does not involve harmful chemicals, capping/reducing agents, or severe treatments. This approach is quite novel, simple, and green.

Optical Studies. The UV–visible diffuse absorbance (Figure 2a) and reflectance spectra (Figure S2, Supporting

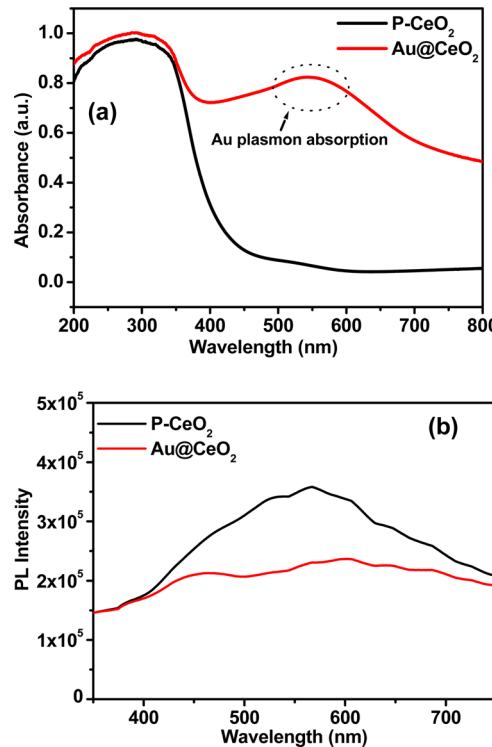


Figure 2. (a) UV–vis diffuse absorption spectra and (b) photoluminescence spectra of Au@CeO₂ nanocomposite and P-CeO₂.

Information, SI) of the Au@CeO₂ nanocomposite and P-CeO₂ were measured to determine their light absorption characteristics. The wavelength distribution of the absorbed light is an important property of photocatalysts, irrespective of the quantum yield. The high absorption of Au@CeO₂ nanocomposite was attributed to the higher visible light absorbance, as indicated by the UV–visible diffuse absorption spectra (Figure 2a). The Au@CeO₂ nanocomposite showed typical absorption due to a band gap transition in the range, 500–600 nm, that is, in the visible region, which is caused by the surface plasmon band characteristics of gold.^{19,20} This further confirms that the AuNPs had been anchored/adsorbed successfully at the surface of P-CeO₂. The extended absorbance of the Au@CeO₂ nanocomposite in the visible region, which is the typical surface plasmon band exhibited by the AuNPs, confirmed that Au@CeO₂ nanocomposite has considerable applied importance due to the efficient utilization of visible light. The red-shifted absorption spectrum provides evidence of the interaction

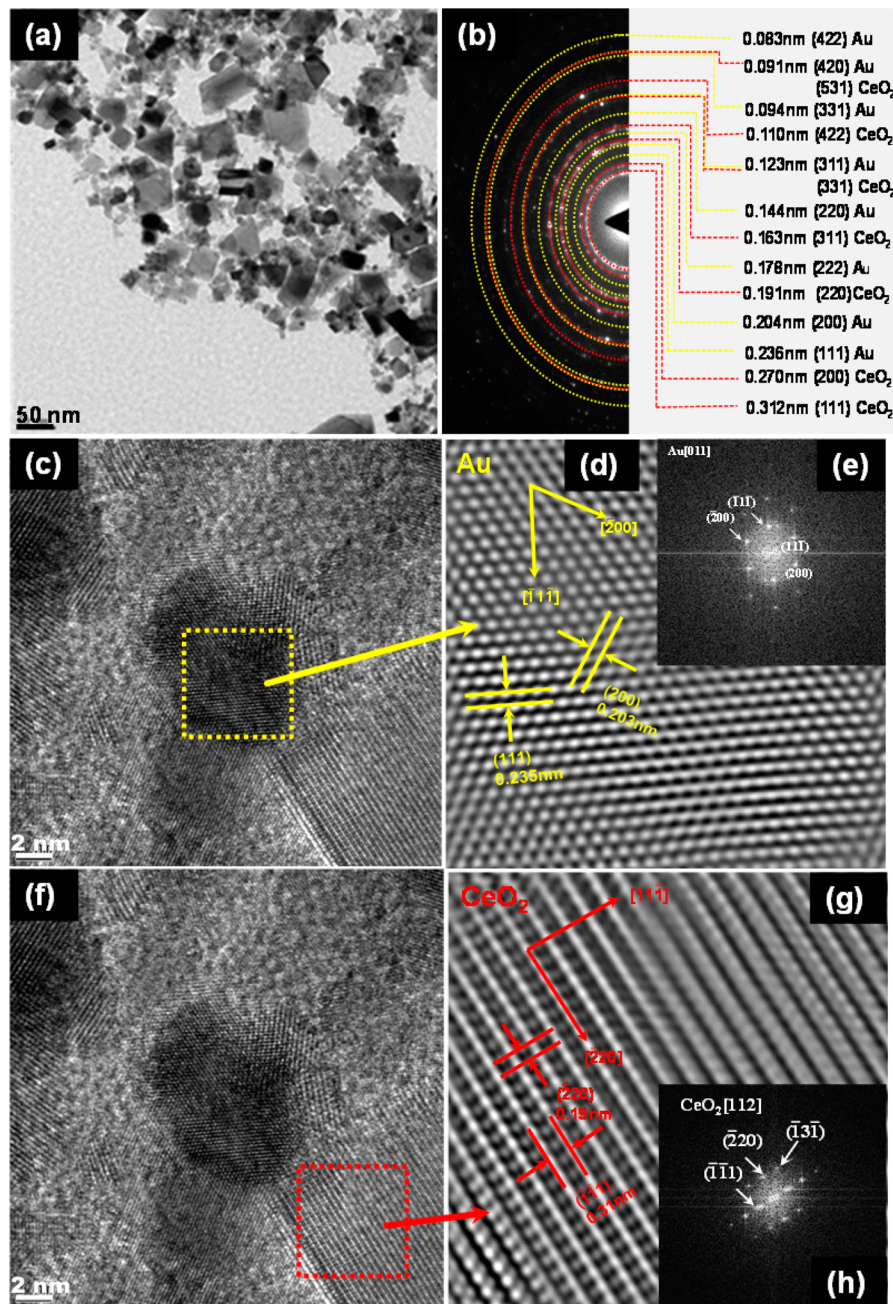


Figure 3. (a) TEM image; (b) SAED pattern; (c) HR-TEM image, dotted area showing the AuNPs; (d) digital diffractogram taken from the region indicated by the dotted box (yellow) showing the AuNPs; (e) inverse FFT image from the region indicated by the dotted box (yellow), that is, Au; (f) HR-TEM, image, dotted area showing CeO₂; (g) digital diffractogram taken from the region indicated by the dotted box (red) showing CeO₂; and (h) inverse FFT image from the region indicated by the dotted box (red), that is, CeO₂ of Au@CeO₂ nanocomposite.

between Au and CeO₂, which is also in accordance with other studies.^{11,12}

Photoluminescence (PL) measurements were performed to determine the charge recombination and migration efficiency of the Au@CeO₂ nanocomposite and P-CeO₂ because the photocatalytic activity is related closely to the PL intensity and the recombination rate of photoexcited electrons and holes. Figure 2b shows the PL spectra of the Au@CeO₂ nanocomposite and P-CeO₂ measured at an excitation wavelength of 325 nm. The emission intensity of the PL spectrum of the Au@CeO₂ nanocomposite was lower than that of P-CeO₂, suggesting that the anchoring of AuNPs to the CeO₂ surface could quench the fluorescence from the CeO₂ nanoparticles and prolong the

electron–hole pair lifetime.^{11,12,21} A lower photoluminescence intensity means a lower electron–hole recombination rate and, hence, a longer lifetime of the photogenerated carriers.^{11,12,21} In general, efficient charge separation and inhibited electron–hole recombination by AuNPs are favorable for enhancing the photocatalytic activity of P-CeO₂. The PL spectra showed that the anchoring of AuNPs to the CeO₂ surface could effectively inhibit electron and hole recombination during the photocatalytic reaction under visible light irradiation.

Transmission Electron Microscopy. TEM and HR-TEM analysis was performed to analyze the microstructure of the Au@CeO₂ nanocomposite (Figure 3). The shapes of the CeO₂ particles are nonuniform, with a majority observed as cubes.

Triangular and diamond-shaped particles were also visible in the TEM image. The size of the particles was in the range of 20 to 30 nm. The difference in contrast (Figure 3a) suggests that the AuNPs has anchored/adsorbed at the surface of CeO₂. This inference was confirmed by EDX analysis of different regions of the Au@CeO₂ catalyst (Figure S3, SI). Figure S4, shows the HAADF-STEM image of Au@CeO₂. The AuNPs appear to be dispersed relatively uniformly and anchored to the surface of CeO₂, forming the Au@CeO₂ nanocomposite. Figures 3b and S5 show the selected area electron diffraction (SAED) pattern of Au@CeO₂, suggesting the sample has a polycrystalline structure, which is in accordance with the XRD result (Figure 4). The diffraction reflections in the electron diffraction pattern

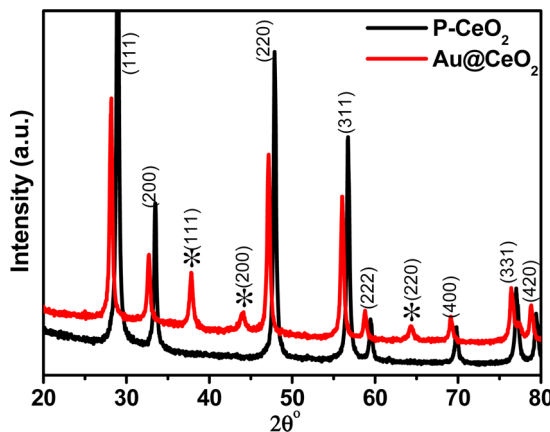


Figure 4. XRD patterns of the Au@CeO₂ nanocomposite and P-CeO₂. The peaks marked with (*) represent the Au signals.

obtained by SAED revealed a polycrystalline structure. Two phases were observed with face centered cubic (fcc) lattices; Au (yellow dotted line; the space group $Fm\bar{3}m$, the lattice parameter $a = 0.408$ nm; Figure 3c), and CeO₂ (Figure 3f; red dotted line; the space group $Fm\bar{3}m$, the lattice parameter $a = 0.5418$ nm). Figure 3c,f shows the typical profile view of a HRTEM image of an AuNPs with a CeO₂ matrix. The HRTEM image revealed the anchoring of AuNPs at CeO₂ along with an interface with the continuity of lattice fringes between the AuNPs and CeO₂. Au has a low-index (111) facet. The reflection of Au was identified through fast Fourier transformed (FFT) digital diffractograms (Figure 3e) obtained in the atomic resolution image. The image, which was recorded along the [011] zone axis, clearly shows the single crystal structure of AuNPs. Figure 3d was obtained after applying the inverse Fourier transform, which clearly shows lattice spacing. Using the Miller-Bravais indices (hkl) for gold reflections such as (111) and (200), were observed, which have a lattice spacing of 0.235 and 0.203 nm, respectively. The image (Figure 3g), which was recorded along the [112] zone axis, clearly shows the single crystal structure of CeO₂ particles, whereas Figure 3h shows an enhanced contrast filtered image of CeO₂. Using the Miller-Bravais indices (hkl) for CeO₂ reflections, such as the (111) and (220), which have a lattice spacing of 0.310 and 0.193 nm, respectively, were obtained. As shown in Figure 3c,f, the size of AuNPs is in the range of 6–10 nm, suggesting that, during the formation of the Au@CeO₂ nanocomposite, the AuNPs were not subjected to significant aggregation. This suggests that the intrinsic nature of noble metal nanoparticles plays a key role in the formation of Au@CeO₂ nanocomposite. In other words, the AuNPs are robust enough that they can resist the significant

aggregation during the formation of Au@CeO₂ nanocomposite and are anchored evenly at the surface of CeO₂.

X-ray Diffraction. Figure 4 shows the XRD patterns of the Au@CeO₂ nanocomposite and P-CeO₂, in which the unmarked peaks were indexed to the well crystalline face centered cubic structure of CeO₂ corresponding to JCPDS (34–0394), whereas the other peaks at 37.78, 44.13, and 64.27° marked with “*” were assigned to face centered cubic (fcc) gold (111), (200), and (220) planes corresponding to JCPDS (04–0784), respectively. The peaks at 28.54, 33.08, 47.48, 56.33, 59.08, 69.4, 76.69, and 79.06° 2θ were assigned to the CeO₂ (111), (200), (220), (311), (222), (400), (331), and (420) planes, respectively. The XRD pattern of the Au@CeO₂ nanocomposite after Au anchoring on CeO₂ was similar to P-CeO₂ except for a minor shift toward a lower angle. This suggests that the AuNPs were not incorporated into the CeO₂ lattice and, instead, were anchored at the surface of CeO₂. Makinson et al. reported that faulted nanocrystals showed peak shift due to the effects of stacking faults.^{11,22} Stacking faults causes stress in the crystal lattice and this stress is responsible for minor shift in the XRD peak toward lower angle. In the present case too, stacking faults appear to be responsible for the peak shift. The crystallite size of the Au@CeO₂ nanocomposite and P-CeO₂ calculated using the Scherrer formula was ~28.5 and ~25 nm, respectively.²³ The increase in the crystallite size of the Au@CeO₂ nanocomposite compared to the P-CeO₂ might be due to the anchoring of very small AuNPs at the surface of P-CeO₂, which is also clear from the HRTEM image (Figure 3).

XPS Analysis of Au@CeO₂ Nanocomposite. The surface chemical composition and chemical states of the Au@CeO₂ nanocomposite was investigated by XPS. Figure S6 presents the XPS survey spectra of Au@CeO₂ nanocomposite showing that the material contains only Au, Ce, and O, as well as C, and no other impurity elements were observed. The atomic % of Au 4f, Ce 3d5, and O 1s was found to be 0.4, 18.7, and 80.9%, respectively. Figure S6 shows the Ce 3d spectra with specific peaks at 883.82 eV for $3d_{5/2}$ and 901.88 eV for $3d_{3/2}$, indicating the oxidation state of Ce⁴⁺ in the form of CeO₂ in the materials. Figure S6 also presents the core level Au 4f⁷ spectra of the AuNPs in Au@CeO₂ nanocomposites at 84.00 eV, which is an evidence of the reduction of Au³⁺ ions by EAB to produce metallic gold. This study is further supported by EDX analysis of Au@CeO₂ nanocomposite (Figure S3, SI).

Electrochemical Studies of Au@CeO₂ Nanocomposite and P-CeO₂. Electrochemical Impedance Spectroscopy. EIS was used to examine the Au@CeO₂ nanocomposite and P-CeO₂ in the dark and under visible light irradiation to understand the visible light photoactivity of the prepared photoelectrodes. The interface charge separation efficiency of the photogenerated electrons and holes is a crucial factor for the photocatalytic activity. The interface charge separation efficiency can be examined by EIS Nyquist plot. Figure 5a shows the EIS Nyquist plots of the Au@CeO₂ nanocomposite and P-CeO₂ in dark and under visible light irradiation. The arc radius of the EIS Nyquist plot of the Au@CeO₂ nanocomposite was smaller than that of P-CeO₂ in the dark and under visible light irradiation. More effective separation of photogenerated electron–hole pairs and faster interfacial charge transfer is believed to have occurred on the Au@CeO₂ nanocomposite under this condition because the arc radius of the EIS spectra reflects the interface layer resistance occurring at the electrode surface.^{12,14,24} These results clearly show that the interaction of

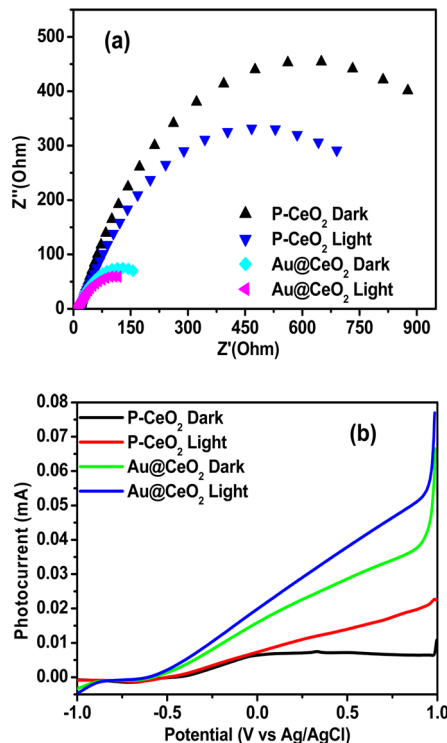


Figure 5. (a) EIS Nyquist plots and (b) photocurrent measurements by LSV for the Au@CeO₂ nanocomposite and P-CeO₂ under dark and visible light irradiation.

AuNPs and CeO₂ could effectively enhance the separation and transfer efficiency of the photogenerated electron–hole pairs in the Au@CeO₂ nanocomposite.^{12,24,25} This data supports the DRS and PL results. EIS confirmed that the Au@CeO₂ nanocomposite can be used as an effective material for photoelectrodes.

Linear Scan Voltammetry (LSV). LSV was performed in the dark and under visible light irradiation to further examine the visible light response of the Au@CeO₂ nanocomposite and P-CeO₂, as shown in Figure 5b.^{24,26,27} The photocurrent of Au@CeO₂ nanocomposite increased gradually compared to P-CeO₂, which suggests that the AuNPs at CeO₂ can effectively improve the photoconversion efficiency and light harvesting ability of CeO₂. Generally, a high photocurrent suggests that the sample has strong ability to generate and transfer the photoexcited charge carriers under irradiation.²⁴ The increased photocurrent also shows an increase in the transport rate of photoinduced carriers and an improvement of photogenerated electron–hole pair separation.^{24–27} Moreover, the extent of electron–hole recombination in the Au@CeO₂ nanocomposite and P-CeO₂ is also supported by the PL measurements (Figure 2b). This shows that the AuNPs can effectively suppress the recombination of photogenerated electron–hole pairs and enhance the photocatalytic activity of Au@CeO₂ nanocomposite.²⁶ Overall, these results show that the Au@CeO₂ nanocomposite can serve as effective materials for increasing the photocurrent.

Visible Light Induced Photocatalytic Degradation of MO and MB. Figure 6 shows the photocatalytic performance of the Au@CeO₂ photocatalyst and P-CeO₂ for the catalytic degradation of MO and MB under visible light irradiation as a model dye. The kinetic curves of photodegradation (Figure 6) compared to P-CeO₂ showed that the Au@CeO₂ photocatalyst promotes the photodegradation of MO and MB under visible

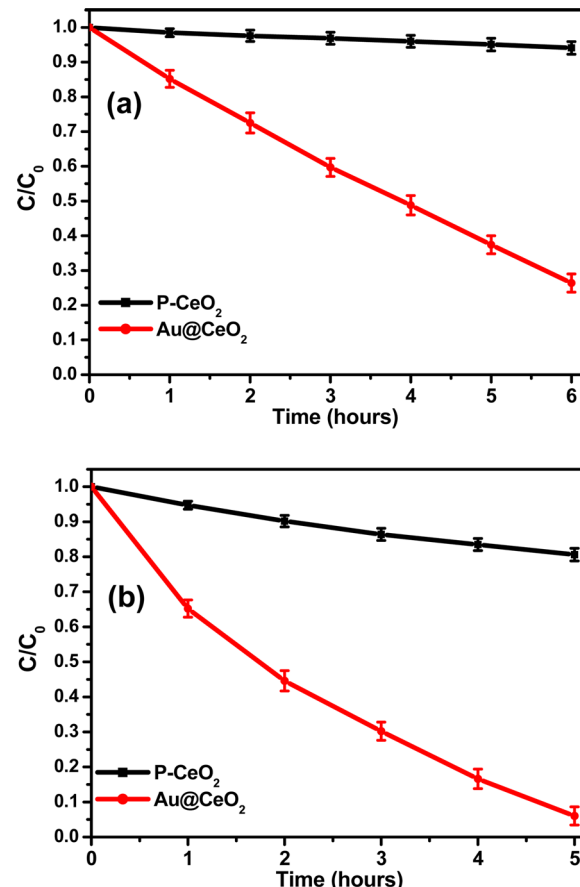


Figure 6. Photocatalytic degradation of (a) MO and (b) MB by the Au@CeO₂ photocatalyst and P-CeO₂.

light irradiation due to the charge separation and visible light harvesting properties of the AuNPs. Approximately 80% MO and 95% MB were degraded after 6 and 5 h, respectively, under visible light irradiation in the presence of the Au@CeO₂ photocatalyst compared to P-CeO₂. The higher observed photocatalytic activity of the Au@CeO₂ photocatalyst compared to P-CeO₂ suggests that the AuNPs were anchored at the surface of P-CeO₂ and behave as an electron sink, which can increase the separation of the photogenerated electron–hole pairs significantly and inhibit their recombination.^{11,12,21,28,29} This suggests that the small size of AuNPs at the surface of P-CeO₂ enhanced the photocatalytic activity of P-CeO₂ for effective dye degradation under visible light irradiation.

Figure 7 shows the proposed mechanism of the photo-induced charge separation, migration, and degradation process

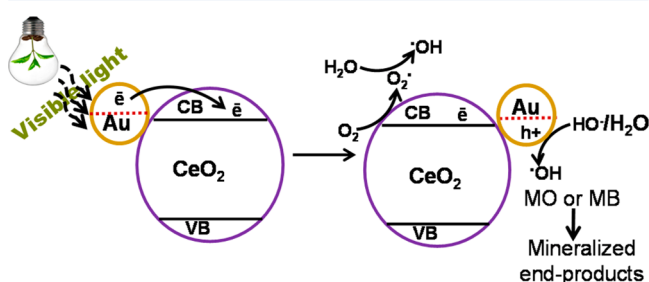


Figure 7. Proposed mechanism for the visible light induced degradation of MO and MB by the Au@CeO₂ photocatalyst.

of MO and MB under visible light irradiation. The observed differences in the photocatalytic activities of the Au@CeO₂ photocatalyst and P-CeO₂ can be explained based on the light harvesting ability of the Au@CeO₂ nanocomposite. The Fermi energy of the AuNPs was higher than that of CeO₂.³ This leads to the transfer of electrons from the Fermi level of Au to the Fermi level of CeO₂, until the two levels reach equilibrium and form an equilibrated Fermi energy level.³⁰ The Fermi levels of Au and CeO₂ were adjusted to the new values during the formation of the Au@CeO₂ photocatalyst.³¹ During visible light irradiation, the equilibrated Fermi level electrons were injected rapidly into the CeO₂ conduction band via a surface plasmon resonance (SPR) mechanism. These injected electrons were trapped by dissolved oxygen molecules in water to yield high oxidative species, such as superoxide radical anions ($\bullet\text{O}_2^-$) and hydroxyl radicals (HO \bullet).^{32–34} The AuNPs in contact with P-CeO₂ facilitates electron–hole separation and then assists in the formation of hydroxyl radicals. The superoxide radical anions ($\bullet\text{O}_2^-$) and hydroxyl radicals (HO \bullet) produced under visible light irradiation might be responsible for the mineralization of organic pollutants.^{12,28} Charge separation was also revealed by the decrease in the PL intensity of the Au@CeO₂ photocatalyst compared to P-CeO₂. In general, photogenerated electrons can react with the oxygen molecules adsorbed on the surface of the Au@CeO₂ photocatalyst to yield $\bullet\text{O}_2^-$. Therefore, Au@CeO₂ photocatalyst showed enhanced visible light photocatalytic activity compared to P-CeO₂ and other reported metal–metal oxide nanocomposites.^{4,11,12} Moreover, the photocatalytic activity has a positive correlation with the reactive radical formation rate, that is, the faster formation of radicals leads to higher photocatalytic activity of the catalyst.^{21,24,32–34} Finally, these results suggest that AuNPs at the surface of CeO₂ will help increase the rate of formation of $\bullet\text{O}_2^-$ and HO \bullet reactive radicals and simultaneously assist in the degradation of organic pollutants. Therefore, Au@CeO₂ nanocomposite could also be used as an effective visible light active photocatalyst.

Stability and Reusability of the Au@CeO₂ Nanocomposite. The stability of the Au@CeO₂ nanocomposite was evaluated by the irradiation of an aqueous suspension of Au@CeO₂ nanocomposite with visible light and sonicated for 1 h. The solution was later analyzed for any leached gold using a UV–visible spectrophotometer (SI, Figure S7), but the analysis did not show any absorbance for gold. This confirms that the Au@CeO₂ nanocomposite was quite stable. The reusability of the Au@CeO₂ nanocomposite was tested by centrifuging the catalyst from the dye solutions, washing with DI water, and drying in an air oven at 100 °C. The reused catalyst showed ~95% and ~90% response for second and third run respectively, to that of the fresh catalyst (Figure S8), which highlights the stability and reusability of the Au@CeO₂ nanocomposite.

CONCLUSIONS

This study reported the biogenic fabrication of Au@CeO₂ nanocomposite and their enhanced visible light photoactivity. The synthesis of the Au@CeO₂ nanocomposite was confirmed by UV–visible, PL, XRD, XPS, and TEM analysis, whereas the enhanced visible light photoactivity was confirmed by photoelectrochemical and photocatalytic studies. The EIS and LSV response under visible light irradiation showed enhanced performance in contrast to P-CeO₂. The as-synthesized Au@CeO₂ nanocomposite also showed the high stability, reusability

and enhanced visible light photocatalytic activities in degrading MO and MB compared to P-CeO₂. The proposed approach provides a novel route for the synthesis of nanocomposites with enhanced visible light activities that can be used repeatedly for a variety of visible light active applications.

ASSOCIATED CONTENT

S Supporting Information

Additional information is presented, such as, UV–vis DRS spectra, SAED, HAADF, EDX, and XPS survey spectra of Au@CeO₂ nanocomposite, UV–vis spectra of Au@CeO₂ for Au leaching. This material is available free of charge via the Internet at <http://pubs.acs.org>.

AUTHOR INFORMATION

Corresponding Author

*Tel.: +82-53-810-2517. Fax: +82-53-810-4631. E-mail: mhcho@ynu.ac.kr.

Notes

The authors declare no competing financial interest.

ACKNOWLEDGMENTS

This study was supported by Basic Science Research Program through the National Research Foundation of Korea (NRF) funded by the Ministry of Education, Science and Technology (Grant No. 2012R1A1A4A01005951).

REFERENCES

- (1) Abe, R. Recent Progress on Photocatalytic and Photoelectrochemical Water Splitting under Visible Light Irradiation. *J. Photochem. Photobiol. C* **2010**, *11*, 179–209.
- (2) Zhang, N.; Liu, S.; Fu, X.; Xu, Y. J. A Simple Strategy for Fabrication of “Plum-Pudding” Type Pd@CeO₂ Semiconductor Nanocomposite as a Visible-Light-Driven Photocatalyst for Selective Oxidation. *J. Phys. Chem. C* **2011**, *115*, 22901–22909.
- (3) Sun, C.; Li, H.; Chen, L. Nanostructured Ceria-Based Materials: Synthesis, Properties, and Applications. *Energy Environ. Sci.* **2012**, *5*, 8475–8505.
- (4) Na, T.; Jingyue, L.; Wenjie, S. Tuning the Shape of Ceria Nanomaterials for Catalytic Applications. *Chin. J. Catal.* **2013**, *34*, 838–850.
- (5) Tanaka, A.; Hashimoto, K.; Kominami, H. Preparation of Au/CeO₂ Exhibiting Strong Surface Plasmon Resonance Effective for Selective or Chemoselective Oxidation of Alcohols to Aldehydes or Ketones in Aqueous Suspensions under Irradiation by Green Light. *J. Am. Chem. Soc.* **2012**, *134*, 14526–14533.
- (6) Chueh, W. C.; Hao, Y.; Jung, W. C.; Haile, S. M. High Electrochemical Activity of the Oxide Phase in Model Ceria–Pt and Ceria–Ni Composite Anodes. *Nat. Mater.* **2012**, *11*, 155–161.
- (7) Primo, A.; Marino, T.; Corma, A.; Molinari, R.; García, H. Efficient Visible-Light Photocatalytic Water Splitting by Minute Amounts of Gold Supported on Nanoparticulate CeO₂ Obtained by a Biopolymer Templating Method. *J. Am. Chem. Soc.* **2011**, *133*, 6930–6933.
- (8) Wu, Y. Y.; Mashayekhi, N. A.; Kung, H. H. Au–Metal Oxide Support Interface as Catalytic Active Sites. *Catal. Sci. Technol.* **2013**, *3*, 2881–2891.
- (9) Corma, A.; Atienzar, P.; Garcia, H.; Ching, J. C. Hierarchically Mesostructured Doped CeO₂ with Potential for Solar-Cell Use. *Nat. Mater.* **2004**, *3*, 394–397.
- (10) Chen, H.; Nanayakkara, C. E.; Grassian, V. H. Titanium Dioxide Photocatalysis in Atmospheric Chemistry. *Chem. Rev.* **2012**, *112*, 5919–5948.
- (11) Khan, M. M.; Ansari, S. A.; Lee, J.; Cho, M. H. Highly Visible Light Active Ag@TiO₂ Nanocomposites Synthesized by Electrochemi-

- cally Active Biofilm: A Novel Biogenic Approach. *Nanoscale* **2013**, *5*, 4427–4435.
- (12) Ansari, S. A.; Khan, M. M.; Ansari, M. O.; Lee, J.; Cho, M. H. Biogenic Synthesis, Photocatalytic, and Photoelectrochemical Performance of Ag–ZnO Nanocomposite. *J. Phys. Chem. C* **2013**, *117*, 27023–27030.
- (13) Khan, M. M.; Lee, J.; Cho, M. H. Electrochemically Active Biofilm Mediated Bio-Hydrogen Production Catalyzed by Positively Charged Gold Nanoparticles. *Int. J. Hydrogen Energy* **2013**, *38*, 5243–5250.
- (14) Ansari, S. A.; Khan, M. M.; Kalathil, S.; Nisar, A.; Lee, J.; Cho, M. H. Oxygen Vacancy Induced Band Gap Narrowing of ZnO Nanostructures by an Electrochemically Active Biofilm. *Nanoscale* **2013**, *5*, 9238–9246.
- (15) Kalathil, S.; Khan, M. M.; Lee, J.; Cho, M. H. Production of Bioelectricity, Bio-Hydrogen, High Value Chemicals and Bioinspired Nanomaterials by Electrochemically Active Biofilms. *Biotechnol. Adv.* **2012**, *31*, 915–924.
- (16) Han, T. H.; Khan, M. M.; Kalathil, S.; Lee, J.; Cho, M. H. Simultaneous Enhancement of Methylene Blue Degradation and Power Generation in a Microbial Fuel Cell by Gold Nanoparticles. *Ind. Eng. Chem. Res.* **2013**, *52*, 8174–8181.
- (17) Khan, M. M.; Ansari, S. A.; Lee, J.; Cho, M. H. Mixed Culture Electrochemically Active Biofilms and their Microscopic and Spectroelectrochemical Studies. *ACS Sustainable Chem. Eng.* **2014**, *2*, 423–432.
- (18) Khan, M. M.; Ansari, S. A.; Lee, J.; Cho, M. H. Novel Ag@TiO₂ Nanocomposite Synthesized by Electrochemically Active Biofilm for Nonenzymatic Hydrogen Peroxide Sensor. *Mater. Sci. Eng., C* **2013**, *33*, 4692–4699.
- (19) Yang, Y.; Li, L.; Li, W. Plasmon Absorption of Au-in-CoAl₂O₄ Linear Nanopeapod Chains. *J. Phys. Chem. C* **2013**, *117*, 14142–14148.
- (20) Link, S.; El-Sayed, M. A. Size and Temperature Dependence of the Plasmon Absorption of Colloidal Gold Nanoparticles. *J. Phys. Chem. B* **1999**, *103*, 4212–4217.
- (21) Liqiang, J.; Yichun, Q.; Baiqi, W.; Shudan, L.; Baojiang, J.; Libin, Y.; Wei, F.; Honggang, F.; Jiazhong, S. Review of Photoluminescence Performance of Nano-Sized Semiconductor Materials and Its Relationships with Photocatalytic Activity. *Sol. Energy Mater. Sol. Cells* **2006**, *90*, 1773–1787.
- (22) Makinson, J. D.; Lee, J. S.; Magner, S. H.; Angelis, R. J. D.; Weins, W. N.; Hieronymus, A. S. X-Ray Diffraction Signatures of Defects in Nanocrystalline Materials. *Adv. X-ray Anal.* **2000**, *42*, 407–411.
- (23) Cullity, B. D.; Stock, S. R. *Elements of X-ray Diffraction*; Prentice Hall: NJ, 2001.
- (24) Khan, M. M.; Ansari, S. A. A.; Pradhan, D.; Omaish, M.; Han, D. H.; Lee, J.; Cho, M. H. Band Gap Engineered TiO₂ Nanoparticles for Visible Light Induced Photoelectrochemical and Photocatalytic Studies. *J. Mater. Chem. A* **2014**, *2*, 637–644.
- (25) Wang, Y.; Shi, R.; Lin, J.; Zhu, Y. Significant Photocatalytic Enhancement in Methylene Blue Degradation of TiO₂ Photocatalysts via Graphene-Like Carbon In Situ Hybridization. *Appl. Catal., B* **2010**, *100*, 179–183.
- (26) Wang, T.; Jiao, Z.; Chen, T.; Li, Y.; Ren, W.; Lin, S.; Lu, G.; Ye, J.; Bi, Y. Vertically Aligned ZnO Nanowire Arrays Tip-Grafted with Silver Nanoparticles for Photoelectrochemical Applications. *Nanoscale* **2013**, *5*, 7552–7557.
- (27) Gan, J.; Lu, X.; Wu, J.; Xie, S.; Zhai, T.; Yu, M.; Zhang, Z.; Mao, Y.; Wang, S. C.; Shen, Y.; Tong, Y. Oxygen Vacancies Promoting Photoelectrochemical Performance of In₂O₃ Nanocubes. *Sci. Rep.* **2013**, *3*, 1021–1028.
- (28) Wang, P.; Huang, B.; Dai, Y.; Whangbo, M. H. Plasmonic Photocatalysts: Harvesting Visible Light with Noble Metal Nanoparticles. *Phys. Chem. Chem. Phys.* **2012**, *14*, 9813–9825.
- (29) Kalathil, S.; Khan, M. M.; Banerjee, A. N.; Lee, J.; Cho, M. H. A Simple Biogenic Route to Rapid Synthesis of Au@TiO₂ Nano-
- composites by Electrochemically Active Biofilms. *J. Nanopart. Res.* **2012**, *14*, 1051–1060.
- (30) Zheng, Y.; Chen, C.; Zhan, Y.; Lin, X.; Zheng, Q.; Wei, K.; Zhu, J. Photocatalytic Activity of Ag/ZnO Heterostructure Nanocatalyst: Correlation Between Structure and Property. *J. Phys. Chem. C* **2008**, *112*, 10773–10777.
- (31) Sangpour, P.; Hashemi, F.; Moshfegh, A. Z. Photoenhanced Degradation of Methylene Blue on Cospattered M:TiO₂ (M = Au, Ag, Cu) Nanocomposite Systems: A Comparative Study. *J. Phys. Chem. C* **2010**, *114*, 13955–13961.
- (32) Liqiang, J.; Zhou, W.; Tian, G.; Fu, H. Surface Tuning for Oxide-Based Nanomaterials as Efficient Photocatalysts. *Chem. Soc. Rev.* **2013**, *42*, 9509–9549.
- (33) Ansari, S. A.; Khan, M. M.; Ansari, M. O.; Lee, J.; Cho, M. H. Highly Photoactive SnO₂ Nanostructures Engineered by Electrochemically Active biofilm. *New J. Chem.* **2014**, DOI: 10.1039/C3NJ01488F.
- (34) Ansari, S. A.; Khan, M. M.; Ansari, M. O.; Kalathil, S.; Lee, J.; Cho, M. H. Band Gap Engineering of CeO₂ Nanostructure Using an Electrochemically Active Biofilm for Visible Light Applications. *RSC Adv.* **2014**, *4*, 16782–16791.